Review Article

Open Access

Ana Ballestar, Pablo Esquinazi*

Transport characteristics of focused beam deposited nanostructures

Abstract: We review the transport properties of different nanostructures produced by ion- and electron-beam deposition, as prepared as well as after certain treatments. In general, the available literature indicates that the transport properties are determined by conduction processes typical for disordered metallic grains embedded in a carbon-rich matrix, including intergrain tunneling and variable range hopping mechanisms. Special emphasis is given to the superconducting behavior found in certain Tungsten-Carbide nanostructures that, in a certain field and temperature range, is compatible with that of granular superconductivity. This granular superconductivity leads to phenomena like magnetic field oscillations as well as anomalous hysteresis loops in the magnetoresistance.

1 Introduction

The increasing interest on devices with dimensions in the order of nanometers lead to the development of new technologies in the area of nano-prototyping and nanofabrication. The reduced dimensions in micro- and nanoelectronics come along with a large complexity of device processing. In case of any failure in the preparation of the structures, a tool able to modify and repair the interconnections in the device is required. The deposition of nanostructures by means of focused beam (FB) is an attractive approach to the formation of complex and small connections. It is a direct-writing, single step process technique with resolution comparable to the structures defined by electron-beam lithography. The process is based on the local decomposition of gaseous precursors containing the needed element(s). In this way, these precursors are deposited on the sample at the vicinity of the electron or ion beam. The interaction of the electrons or the ions from the beam with the precursor decomposes the molecules. The non-volatile reaction product is deposited on the surface inducing localized deposits and part of the organic volatile fragments diffuse away and are exhausted out of the system. This growth mechanism is considered to be a chemical vapor deposition (CVD) process assisted by a focused-electron-beam (FEB) or a focused-ion-beam (FIB). They are the so-called focused electron beam deposition (FEBID or simply EBID) and the focused ion beam deposition (FIBID or IBID).

The FB based processes depend on several parameters that include the beam current, the time the beam remains on the spot (i.e. beam dwell time), raster refresh time, the relative distance between beam positions (usually defined by a percentage, the so-called overlap), the gas used as precursor, its flux and temperature before injection. The adjustment of these parameters is the key to achieve optimum results in the deposition. Furthermore, as will be described in this review, different results can be obtained just by modifying one single parameter during the deposition process. Therefore, as suggested in [1], a complete list of parameters used during the growth is highly recommended to be explicitly included in publications to achieve the necessary reproducibility. For a complete description of the influence of the selected parameters on the deposited structure, we recommend to consult [1,2]. In this review, we will not address the issue of selecting the adequate parameters for a particular purpose, but we will rather focus on the transport properties that have been found in different nano- and micro-structures deposited using EBID and/or IBID. However, and due to its importance, the precursors used in the experiments we review are also indicated (when given by the authors). It appears reasonable to assume

*Corresponding authors: Pablo Esquinazi: Division of Superconductivity and Magnetism, Institut für Experimentelle Physik II, Universität Leipzig, Linnéstraße 5, D-04103 Leipzig, Germany,
E-mail: esquin@physik.uni-leipzig.de
Ana Ballestar: Division of Superconductivity and Magnetism, Institut für Experimentelle Physik II, Universität Leipzig, Linnéstraße 5, D-04103 Leipzig, Germany

that the electronic properties will be strongly determined by the inner structure of the deposit as well as its chemical composition. Due to the growth mechanism, the deposited material is usually composed of the desired (metallic) element plus carbon and oxygen originated from the incomplete dissociation of the precursor molecules. Hence, to a certain extent the obtained deposits are always contaminated with those elements as well as with gallium ions from the used ion beam (in the case of IBID). On the other hand, the FB technique is a single step, mask-less procedure with certain advantages, like a reduction of the contamination coming from the chemicals and remaining of the resistivity typically used in techniques such as lithography.

Throughout this review, we present some EBID and IBID deposited structures showing metallic, semiconducting, insulating or superconducting behavior. In spite of the advantages of FB deposition, there have been only a few reports on the electrical properties of the fabricated structures. The knowledge of the electrical characteristics of the nano- and microdeposits is of primary importance for their use as interconnections in circuits, electrical contacts in nanodevices or even to be used as nanosized sensors [3]. The FB technique is also of interest as it gives the chance to fabricate versatile submicron structures, which can provide interesting details to the field of electronic transport in nanostructures.

The review is organized as follows: in section 2 we discuss the transport characteristics of the nanostructures deposited using a focused beam, either ion beam (2.1) or electron beam (2.2) where (disordered) metallic and insulating behaviors can be observed. In section 3 special attention is given to the superconducting characteristics of Tungsten-Carbide nanostructures, a disordered material that is one of the very few superconducting alloys, among C-Ga-O [4] and $Mo_xC_yGa_zO_\delta$ [5], that can be prepared with a FB technique, reaching a critical temperature of $T_c = 5$ K.

2 Focused beam deposited nanostructures

The deposits obtained using FB techniques present remarkable differences depending on whether the beam used for the deposition is of electrons or ions. The growth mechanism strongly depends on the interaction between the incident beam, the secondary emission and backscattered beam particles coming from the substrate with the precursor molecules [1]. Obviously, the difference between electrons and ions leads to radically different interactions and, consequently, to different structure and

composition of the deposits. Therefore, we divided this section into two parts: 2.1 deals with the nanostructures deposited by IBID and 2.2 with those deposited using EBID.

2.1 Ion Beam Induced Deposited Samples

Being one of the main interests of the FB technique with applications in electrical circuits, most of the produced IBID nanostructures contain metallic elements, such as platinum, palladium, gold, cobalt, tungsten or iron. As mentioned previously, the final composition of the deposits will show the presence of carbon and gallium, coming from the precursors and the ion beam, respectively. Consequently, these elements will influence the electrical properties of the nanostructures. Although the main purpose is to deposit a highly metallic structure, the composition and the inner lattice structure give rise to different electronic properties, sometimes very far away from being metallic.

We address firstly the study of platinum nanostructures deposited by IBID, one of the most common samples prepared with this technique. One finds a pretty wide discrepancy between the results corresponding to different publications studying the electrical properties of such structures. We summarize here the different mechanisms of conduction proposed for IBID deposited Pt-nanowires.

2.1.1 Disordered metal-carbon composites

De Teresa et al. [6] used the four probes method to study the temperature dependence of the resistance and the current-voltage (I–V) characteristic curves of Pt-IBID nanowires without any contribution from lead or contact resistance. In order to fabricate the nanowires, they used $(CH_3)_3Pt(CpCH_3)$ as precursor. A linear behavior is observed in the I–V curves with a resistance of ~1 kΩ ($\rho \approx 800$ μΩ cm or $\sigma = 1250$ Ω^{-1} cm^{-1}). This value was interpreted as a sign of having a metallic or quasimetallic system, as it is around the minimum metallic conductivity value reported by Mott and Davis [7]. Moreover, the slight increase of the resistivity decreasing temperature suggested a quasimetallic conduction mechanism appropriated for disordered metals, as proposed by Möbius et al. [8].

However, the values obtained for the resistivity of these nanowires are far from that of pure Pt (~10 μΩ cm). The difference arises from the microstructure and the chemical composition. High-resolution transmission

electron microscopy showed that the deposits consisted of Pt single crystals embedded in an amorphous carbon matrix [6]. The energy-dispersive X-ray (EDX) results showed a Ga content around 10%, a Pt content varying from 27% to 17% (depending on the growth beam energy), and the C content was more than 60%. These results corroborate the existence of nanocrystalline Pt metallic inclusions with Ga ions (implanted and disorder inducer) within a carbon matrix of semiconducting character [9,10]. Depending on the ratio between these components, different electronic properties can be observed, as in the case of amorphous semiconducting materials with different degrees of doping [7]. Typically, as the doping level and disorder increase, the appearance of impurity states in the vicinity of the Fermi level and a band of localized states separated from the band of unlocalized states occurs. At low temperatures and low doping level, the dominating mechanism is hopping amongst impurities and the material is insulating. If the doping and disorder levels are high, it can lead to the formation of a band and metallic conduction can be observed in the case of percolation where a network of metallic inclusions is created. Hence, in [6], it is suggested that the transport mechanism is dominated by a carbonaceous matrix, which can be tuned by the different amounts of Pt and Ga inside it.

Going a bit further, Lin et al. [11] found that the conduction mechanism in Pt-nanowires deposited by IBID, and with $(C_5H_5)Pt(CH_3)_3$ as precursor, can be well described by the interference of electron-phonon scattering and elastic electron scattering from boundaries and defects. As done in many other studies, this effect is attributed to the strong disorder in the wires and their high Debye temperature. In spite of their structure, i.e. Pt nanocrystals surrounded by a disordered carbon matrix, the authors in [11] claimed that the wires do not show the expected transport properties of an inhomogeneous system. By studying the magnetoresistance (MR), they found that the wires rather present a behavior close to that of disordered, but homogeneous conductors [12]. They observed weak antilocalization effects at low temperatures, from which they could calculate the electron dephasing length (l_ϕ). The saturation of l_ϕ ~60 nm at T < 1 K and its variation at T > 1 K [13] were taken as a hint indicating that the transport in the wires is similar to the one observed in disordered wires, compatible to theoretical predictions for homogeneous conductors [14]. The variation of ρ at temperatures well above 4.2 K (where electron transport should be dominated by electron-phonon scattering) suggested that the interference mechanism dominates even at room temperature [11].

The electron-electron interaction in Pt-IBID wires (prepared as in [11]) was further investigated by the temperature dependence of the resistance and the MR at temperatures below 10 K [13]. To determine the contribution of weak antilocalization and electron-electron interaction, the variation of the low-field MR of the wire, relative to its value at 4.2 K, was investigated. The results obtained [13] revealed that the MR was dominated by weak antilocalization effects. The observed positive MR (that decreased with temperature) was interpreted as a typical feature of weak antilocalization for systems with strong spin-orbit interaction [14]. As in [11], the phase-breaking length was estimated to be $l\phi$ ~100 nm and a saturation at low temperatures was observed. Furthermore, the conductance showed a quantum correction dominated by the electron-electron interaction (found to be a factor of 4–5 times larger than the weak antilocalization contribution). Such scenario is typically found in disordered metals [15].

Independent studies from Barzola et al. [16] reported also the transport properties on Pt wires produced by IBID (trimethyl[(1,2,3,4,5-ETA.)-1-methyl-2,4-cyclopentadien-1-YL]platinum) used as a precursor). In that work, the temperature and magnetic field dependence of the samples has been compared to that found in disordered or granular conductors. Electron diffraction measurements of those samples indicated the presence of an amorphous structure in the wires. A non-metallic behavior was observed in the temperature dependence of the resistivity that followed $\rho(T) = a - bT^{0.9} + cT^{-0.3}$ with the two temperature dependent terms ascribed to two different scattering processes. On the one hand, the quasi-linear term can arise from the scattering of electrons coming from two different bands and with different effective masses (as shown in amorphous alloys of Ge, Sn or Bi). The other contribution has been related to the inhomogeneous structure of the wire and, hence, to a hopping conduction between metallic (Pt) grains within a disordered carbon-based matrix [16]. The investigated MR was positive and increased decreasing temperature, showing a linear field dependence at T = 4 K. These results reflect the strong influence of the inner structure of the wires and the low metal content in the carbon matrix, which appeared to dominate the behavior of the MR as well as to be responsible for the high resistivity (~$1.8 \times 10^3\,\mu\Omega$ cm) found [16]. A disordered metal conduction mechanism was also found in the resistivity of the FIB-deposited Pt-wires in [17] $(C_5H_5Pt(CH_3)_3)$. In that work, the authors reported a similar high value of the resistivity $\rho \approx 103\,\mu\Omega$ cm.

2.1.2 Intergrain tunneling

In the work by Penate et al. [18] ($C_9H_{16}Pt$ used as precursor), the electrical behavior in Pt-IBID deposited wires was explained by intergrain tunneling in disordered materials. As observed in most of the IBID produced wires, structural analysis of the wire showed a highly disordered material with metal-rich grains (atomic composition 31% Pt and 50% Ga) embedded in a non-metallic matrix of carbon, oxygen and silicon [11]. The study of the temperature dependence of the resistivity revealed a small negative temperature coefficient $\beta = \partial\rho/\partial T < 0$, which is characteristic of disordered materials, Fig. 1a. The investigation of the characteristic I–V curves indicated as well as weakly insulating-like behavior. All the measured I–V curves showed a non-linearity, which increased decreasing temperature. The sum of the obtained data brought the authors in [18] to use the Glazman and Matveev (GM) model [21] to describe the phenomenon they observed. Consistently with the structural analysis,

they assumed that the electrical conduction occurred by means of electron tunneling between Pt- (and Ga-) rich grains through the insulating carbon matrix. The model points out the influence of the Ga ions irradiation together with the small size of the metallic grains, which implies a high percentage of disorder responsible for the weakly insulating-type behavior [18].

2.1.3 Variable Range Hopping

The third mechanism of conduction proposed for IBID prepared Pt-wires is the so-called variable range hopping (VRH). The work by De Marzi et al. [22] measured the temperature dependence of the resistance of Pt-wires, which was successfully fitted to a VRH model, as proposed in the past for disordered materials [23–26]. In this study, the precursor gas used was methylcyclopentadienyl–trimethylplatinum. The large value of resistivity reported in [22] ($\rho = 2200 \pm 100$ $\mu\Omega$ cm) is similar to other reports
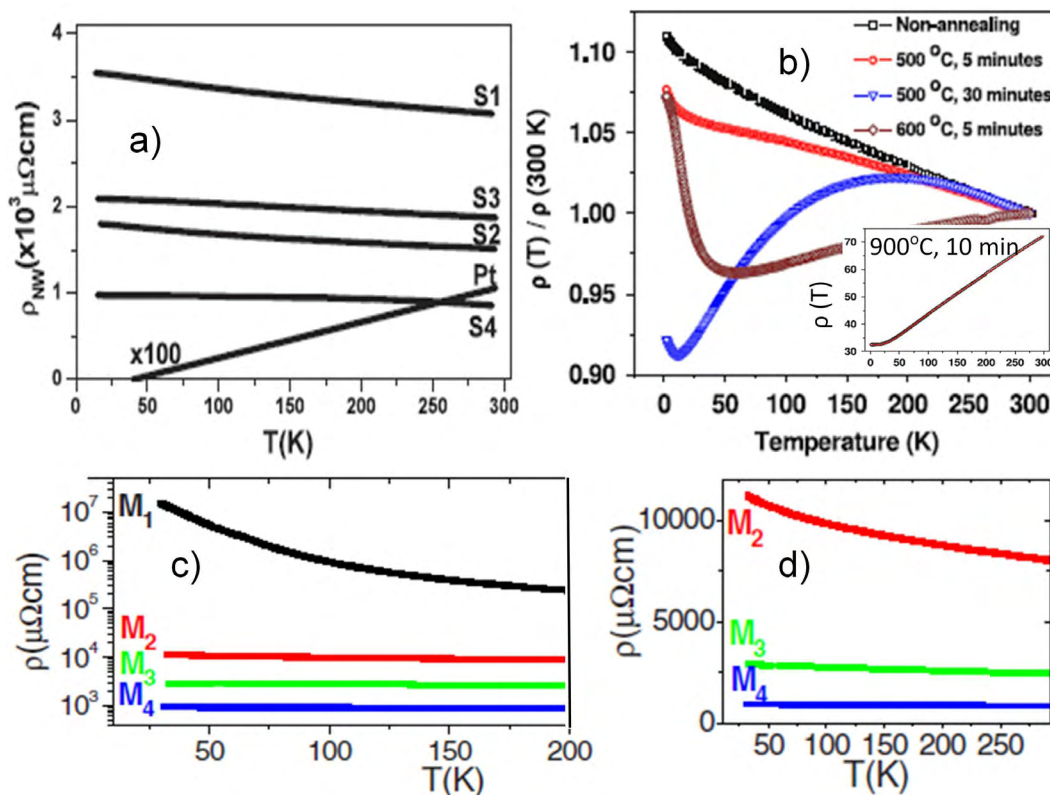
Figure 1: Resistivity vs. temperature of different IBID-prepared Pt-nanowires: a) Four selected nanowires (S1...S4) with different lengths and cross-sectional areas together with the corresponding curve for bulk Pt, adapted from [18] ($C_9H_{16}Pt$ precursor gas); b) normalized resistivity of IBID Pt-nanowires in the as-prepared and after different annealing treatments states, adapted from [19] [$(CH_3)_3CH_3C_5H_4Pt$] as precursor gas]. The inset shows the $\rho(T)$ curve after an annealing at 900°C for 10 min for a Pt-nanowire, adapted from [19]; c) temperature dependence of Pt-nanowires with different thickness. M1 corresponds to the thinnest nanowire (~20 nm) and M4 the thickest one (~190 nm). Increasing the thickness a kind of insulating to disordered transition appears; d) detail of c) in double linear scale. Both figures adapted from [20] [$(CH_3)_3Pt(CpCH_3)$ as precursor gas].

[12,16] and clearly related to the disorder present in the wires. The authors calculated the localization length ($\xi_L < 20$ nm) and using the Anderson theory [27] they stated that the electron wave functions decay rather exponentially over a distance of the order of ξ_L. Hence, one can assume that the intrinsic structural disorder of the IBID deposited Pt-wire is able to "trap" the carriers into localized states.

In order to escape these localized states, the electrons need thermally activated hopping. Similarly, Langford et al. [28] found a negative temperature coefficient for the resistance with a temperature dependence following a $T^{-0.25}$ dependence. The precursor used in their work is methylcyclopentadienyl(trimethyl)platinum. This is the typical behavior of a conduction mechanism dominated by VRH, a mechanism that it is also observed in a large number of different disordered materials, like amorphous matrices doped with nanocrystalline particles [29,30] as well as in single TiO_2 nanotubes [31].

2.1.4 Improving the conductivity of the Pt-nanostructures

In addition to the investigations on as-prepared IBID Pt-wires, different treatment and sample modifications have been done in order to improve the electronic properties of such structures. The effect of annealing on depositions done with $(CH_3)_3CH_3C_5H_4Pt$ as a precursor gas, has been studied by Liao et al. [19]. Important differences on the transport properties of the wires before and after the treatment were observed and are summarized in Table 1 [19].

Fig. 1b presents the normalized resistivity $[\rho(T)/\rho(300 \text{ K})]$ as a function of temperature of the as-deposited Pt/C nanowires and treated ones. One can easily realize the differences between the as-prepared wires and those annealed in different conditions (as indicated in the figure as well as in Table 1). The authors directly correlated the microstructure of the wires with

their transport characteristic. Hence, in the as-prepared wire there exist Pt nanograins located in a Ga+ doped amorphous matrix, which prevents a percolation of the Pt-grains and a granular structure emerges. Therefore, the conduction mechanism is dominated by the contribution of the intergrain tunneling (through the carbon doped matrix) and diffusive intragrain electron motion. The annealing treatment induced a reduction of the disorder and an increase of the grain size, resulting in reduced values of the resistivity ratio $\rho(2 \text{ K})/\rho(300 \text{ K})$ (Table 1) and different $\rho(T)$ dependencies (Fig. 1b).

The resistivity of the as-prepared wires showed a ependence on temperature that followed a $(T)^{1/2}$ at $T < 36$ K, as observed in disordered and granular systems due to quantum interference effects, including weak localization and electron-electron interaction [32,33]. However, the annealed wires no longer followed this law. The authors proved that increasing the annealing temperature (and/or the annealing time) increased the tunneling conductance, as the annealing reduces the degree of disorder. As expected from granular metals with large intergrain conductance, quantum corrections to conductivity originate mainly from local fluctuations of the voltages between neighboring grains [33-37], which dominate the electron transport. That appears to be the case of the wire annealed for 30 min. at 500°C, and this is the phenomena that can explain its characteristic $\rho(T)$ shown in Fig. 1b. Furthermore, the nanowires were improved remarkably when the annealing was done at 900°C for 10 min. The resistivity at room temperature was reduced almost one order of magnitude and the $\rho(T)$ curve showed a "pure metallic" behavior (the inset in Fig. 1b). This points out that the annealing induced the formation of a continuous conductive layer and the conduction mechanism is now dominated by charge transport along coupled metallic grains. The MR showed a crossover from weak antilocalization to weak localization as the sample transformed from granular structures to percolating networks, in agreement with resistivity behavior as a function of temperature. The clear message of the

Table 1: Characteristics of Pt-IBID deposited according to [19]

Sample	Grain diameter	Grain separation	$\rho(2 \text{ K})/\rho(300 \text{ K})$	$\partial\rho/\partial T$
As-deposited	2-4 nm	1-2 nm, isolated	1.111	< 0
500°C, 5 min annealing	3-8 nm	Partial connection	1.077	< 0
500°C, 30 min annealing		Partial connection	0.922	$\partial\rho/\partial T$ (11.5 K < T < 188 K) > 0, otherwise < 0
600°C 5 min annealing		Partial connection	1.073	> 0 (T > 60 K); < 0 (T < 60 K)
900°C annealing	~20 nm	Continuous metal	0.450	> 0

work by Liao et al. [19] is that the electrical conduction in Pt-nanowires produced by IBID can be improved by annealing adequately the samples.

Another way of improving the conductivity of IBID Pt-nanowires is increasing their thickness. Fernandez-Pacheco et al. [20] showed a disordered-metal to insulator transition (MIT) changing the thickness of the wires (prepared using $(CH_3)_3Pt(CpCH_3)$ as precursor gas). In situ measurements of the resistance during deposition showed a decrease in the resistivity from 108 μΩ cm for thickness ~20 nm to a lowest saturated value of 700 μΩ cm for thickness > 150 nm, a behavior already observed in IBID of Pd-nanostructures and W-wires in [38]. The spectroscopy results correlated this reduction with the gradient in the metal-carbon ratio as the thickness of the deposits increased. Moreover, the conduction mechanism was investigated via I–V curves at different temperatures as well as the temperature dependence of the resistivity. The wires with higher metal content (> 33%, thicker ones) showed linear I–V curves with a minimum in the resistivity. In the thinner wires with lower metal content (< 33%), the resistivity was higher and the I–V curves were non-linear. This non-linear effect increased as the temperature was reduced. Using the Glazman-Matveev model [21], the authors in [20] explained this non-linearity in terms of multi-step tunneling occurring between the metallic nanocrystals inside the carbonaceous matrix.

Figs. 1c and 1d show the temperature dependence of the resistivity of different wires (M1 to M4, i.e. thinner to thicker wires) taken from [20]. In the case of the wire M1 (with thickness of ~20 nm) a large negative temperature coefficient is observed and the resistivity follows a thermally activated dependence of the form $\rho(T) = \rho_\infty \exp\left(\frac{T_0}{T}\right)^N$ with N = 0.5. This corresponds to a VRH of electrons between localized states [7] combined with the Coulomb interaction between sites (ES-VHR), which results in a Coulomb gap [39]. In contrast, the ρ(T) curves of M3 and M4 samples indicate a disordered metal conduction as the weak temperature dependence of the resistivity is similar to the one observed in amorphous metals. In this case, the amount of metallic grains is high enough to assure that the transport occurs in extended states. The authors in [20] used the Mott-Anderson theory for noncrystalline materials [7] to explain this transition. Basically, the thicker the wire, the higher the concentration of metal in the carbon matrix, and consequently impurity levels appear in the band gap together with the localization of states in the formed band tails. A further increase of the thickness results finally in a delocalization of the electron wave functions and the system becomes metallic but is highly disordered.

2.1.5 Other materials prepared by IBID

In addition to the Pt-nanostructures, other metallic elements have been deposited using the IBID technique. The case of tungsten [or tungsten-carbide (WC)] will be addressed in a section 3 as they revealed superconducting properties at low temperatures. Studies done in 1986 [40] already reported the IBID of gold, where $C_7H_7F_6O_2Au$ was used as precursor gas. Although the authors claimed to achieve a high content of gold in the deposits (~75%) the resistivity of the films ranged between 5×10^{-4} and 1.3×10^{-3} Ω cm, much higher than the resistivity of bulk Au (2.44×10^{-6} Ω cm). The granularity of the deposits and the presence of gallium (~20%), oxygen (< 5%) and carbon (< 5%) were responsible for the difference in the resistivity values.

Another interesting case are the deposits with palladium. As reported in all the other materials, the structure of the deposits as well as their chemical composition determined the electrical conduction mechanism. Spoddig et al. [38] showed a disordered metal behavior in the Pd-IBID wires with a weakly linear drop of the resistivity decreasing temperature and an absolute value of ρ ~10^{-3} Ω cm. In Pd wires with higher resistivity (ρ ~10^{-2} Ω cm) an upturn in the temperature dependence below 50 K was observed [38]. The change in behavior also appeared in the MR, as in some wires a linear dependence on field was observed, while on others weak localization effects were detected at low temperatures. All these phenomena are related to the non-homogeneous structure of the deposits.

Subsequent studies investigated further the conduction mechanism in Pd samples (palladium bis(hexaflouroacetylacetonate) used as precursor) [16]. The electron diffraction patterns performed in those samples showed a rather polycrystalline structure in contrast to the amorphous pattern in the Pt (or W) deposits. The investigation of the temperature and field dependence of the resistivity gave results pretty similar to those obtained in the Pt-IBID wires. Therefore, the same interpretation was applied to these samples based on the existence of metallic grains embedded in a carbon doped matrix [16].

Magnetic materials have also been an important target of FB deposition techniques. The case of cobalt is of particular interest. Gabureac et al. [3] chose different sets of parameters for the deposition to adjust the size of the Co-nanoparticle size and their relative distance, which they assumed to be the determinant factor on the Hall effect of the Co-C deposits, using IBID as well as with electron beam induced deposition (EBID). Gas molecules of $Co_2(CO)_8$

were used as precursor in the whole study. The authors used the Langevin model to account for the observed paramagnetism and the extraordinary Hall effect (EHE) for sensor characterization purposes. They demonstrated that the granular structure, which enhanced the scattering process, and an optimum nanoparticle size below the superparamagnetic limit, led to a field hysteresis free behavior. This result is of interest because can set the basis for Co-C Hall devices with low-field high sensitivity and nanosize magnetic sensors. Nevertheless, the Co-nanowires produced with EBID appeared more attractive and their properties will be discussed in the next section.

2.2 Electron Beam Induced Deposited Samples

2.2.1 Platinum deposits

In this section, we discuss the transport characteristics of Pt structures prepared using Electron Beam Induced Deposition (EBID). There are several studies about such structures [6,17,28,34,41]. The general trend in all those studies indicates a larger resistivity of EBID Pt-deposits compared with the IBID prepared structures. As in the case of IBID samples, the carbon matrix plays a very important role. However, interesting differences based on a slightly different conduction mechanism are suggested in the literature.

A direct comparison between the resistance behavior as function of temperature for Pt-wires grown using IBID and EBID is shown in Figs. 2a and 2b respectively; following [6]. The first remarkable difference is the resistivity value of the Pt-EBID prepared nanowires, typically four orders of magnitude higher than in Pt-IBID ones, for similar thickness of the deposits (~160 nm). Note that the effect of thickness in the EBID-Pt structures is just a slight decrease in the resistivity, while its effect in IBID-Pt deposits is much larger, section 2.1.4.

The temperature dependence of the resistance of Pt-EBID nanowires (Fig. 2b) is compatible with hopping conduction in a band of localized states inside a semiconducting matrix [35]. A deeper analysis of the conductance (G) showed a linear dependence of $\ln(G)$ versus $T^{1/2}$ at T < 200 K, which is the characteristic dependence of a conduction mechanism dominated by VRH with Coulomb interaction [39]. Again, the obtained results can be ascribed to the internal structure of the wires, i.e. the carbonaceous matrix with the Pt inclusions plays an important role. The difference with the IBID deposits is mainly due to the amount of Ga-ions implantation, which increases the conductivity of the carbon matrix and also the disorder. Hence, the EBID Pt deposits have lower disorder and impurity states. The differences in structure and composition (confirmed by HRTEM and EDX measurements [6]) lead to a conduction mechanism similar to low-doped amorphous semiconductor with a low value of room-temperature conductance and conduction via hopping. A strong increase of the resistance at low temperatures is expected as characteristic of a conduction mechanism via hopping. The study of the I–V curves supported this interpretation; a non-linear behavior was observed and explained with a similar model as used in doped silicon [42,43]. The initial small conductance at low voltages was ascribed to a charge trapping at "dead
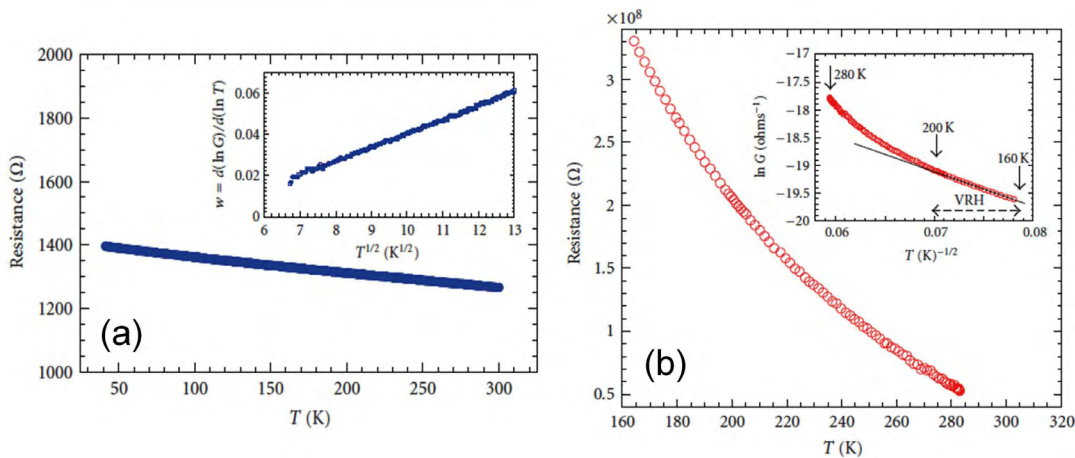
Figure 2: Temperature dependence of the resistance for Pt-nanowires deposited using a) IBID and b) EBID and using $(CH_3)_3Pt(CpCH_3)$ as precursor gas. Both wires have a similar thickness of ~160 nm. The inset in (a) shows the dependence of $w = d(\ln G)/d(\ln T)$ as a function of $T^{1/2}$ (G denotes the conductance). If $w \rightarrow 0$ at low temperatures, the material is expected to behave as a metal [8]. The inset in (b) shows the linear dependence of $\ln(G)$ versus $T^{-1/2}$ for temperatures 200 K > T > 160 K, indicating a VRH conduction mechanism. Adapted from [6].

ends" of the hopping network [6]. A further increase of the applied voltage results in the typical increase in conductance as observed in semiconducting systems with conduction via impurities.

Similar results were presented by Wakaya et al. [17] as the VRH and the Coulomb blockade together dominate the conduction mechanism in their EBID-deposited Pt wires (where $C_5H_5Pt(CH_3)_3$ was the precursor gas used). The resistance dependence on temperature was successfully fitted with the VRH model and the Coulomb oscillations were clearly observed in the gate-voltage dependence of the current [17]. The Pt nanocrystals were considered as the conductive isolated sites embedded in an amorphous carbon matrix. In order to improve the conductivity of the EBID Pt-deposited wires, an annealing at 400°C and 500°C was performed. As a result, the resistance was reduced by 3 to 4 orders of magnitude and a disordered metal-like conduction was observed, similar to the one found in IBID Pt-nanostructures [44]. The MR of the annealed wires showed antilocalization and the electron phase-breaking was found to increase decreasing temperature and to saturate at low temperatures, again similarly to the IBID Pt-deposits and disordered metals.

The results of Langford et al. [28] showed a similar behavior, i.e. annealing at 500°C and Ga+ implantation reduce the resistivity by a factor of 10. Fig. 3 shows the resistivity vs. temperature for the two different deposits,

Pt-IBID and Pt-EBID in Figs. 3a and 3b respectively. In both cases, the temperature coefficient is negative and of similar magnitude. $\rho(T)$ of the Pt-IBID wires was successfully fitted following the model of VRH [22], while in the case of the Pt-EBID wires $\rho(T)$ shows a plateau at T < 50 K, Fig. 3b. The I–V curves were linear in the whole temperature range for Pt-IBID wires, while for the Pt-EBID ones increasingly non-linear I–V curves decreasing temperature were measured. This non-linearity was ascribed to the single electron tunnelling between Pt nanocrystals embedded in the carbon matrix [28]. Transmission electron microscopy results indicated that the size of the Pt-nanocrystals was 6–8 nm and 3–50 nm for the IBID and EBID wires, respectively, Fig. 3c. A difference was observed in the chemical composition being the amount of carbon in the IBID deposits 40–55 at.% and 60–75 at.% in the EBID deposits. Hence, the difference in resistivity and conduction mechanisms are due to the differences in the internal nanostructure, chemical composition plus the presence of Ga in the produced structures.

As a result of the annealing processes, the IBID produced wires were not notably modified, while the EBID deposited wires showed that the grain size increased to 57 nm and the amount of incorporated carbon reduced, resulting in a decrease of the resistivity by a factor of 10 [28]. The resistivity was further decreased by Ga+ implantation giving rise to a radically different behavior
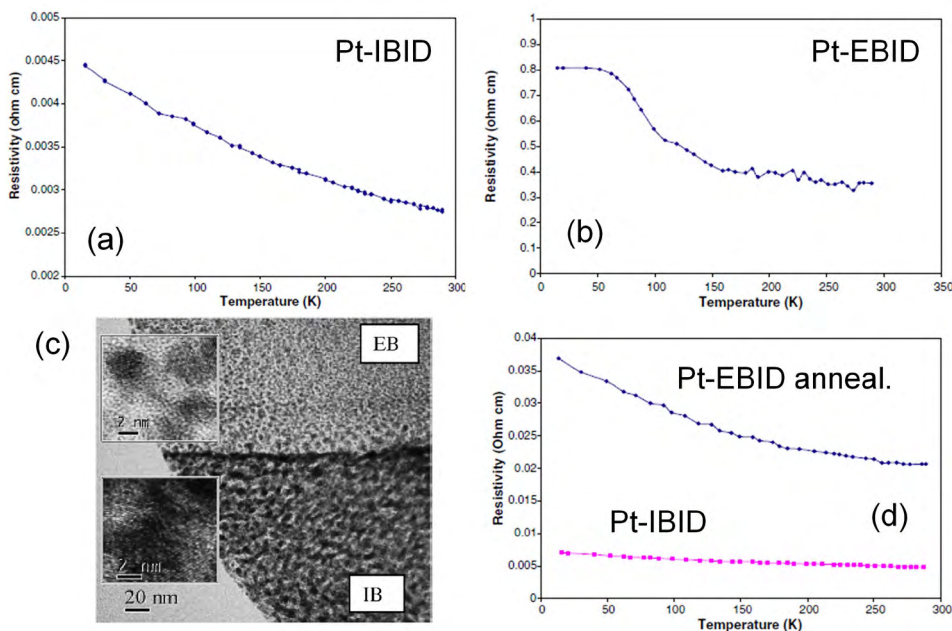
Figure 3: Temperature dependence of the resistivity of Pt-nanowires deposited using: a) IBID and b) EBID; c) bright field and HRTEM (insets) pictures for IBID and EBID Pt-structures (named "IB" and "EB"); d) resistivity vs. temperature for two wires, one prepared using IBID (pink symbols) and another one prepared using EBID, annealed in forming gas for 1 hour at 450°C and implanted with 5 × 10¹⁶ Ga cm⁻². Adapted from [28], where the platinum precursor used was methylcyclopentadienyl(trimethyl) platinum.

than the one showed in Fig. 3b. The plateau vanished and the temperature dependence of the resistivity turned to be similar to that of the IBID deposited Pt wires, Fig. 3d.

Besides the VRH mechanism reported in the above described studies, Fransson et al. [41] investigated the I–V characteristics and interpreted them in terms of tunnelling between the metallic grains. The preparation of the wires was done following the procedure described in [45] where $(C_5H_5)Pt(CH_3)_3$ was the precursor gas used. Analytical and numerical calculations were successfully applied to explain the quadratic variation of the current as a function of the applied voltage found in the experiments.

Finally, Rotkina et al. [34] reported a logarithmic temperature dependence of the conductivity in a wide range of temperature for EBID prepared Pt wires (with $(C_5H_5)Pt(CH_3)_3$ as precursor gas), even after annealing. This dependence was interpreted as due to local fluctuations between metallic grains in a conductive carbon matrix. The authors in [34] claimed that a proper annealing can lead to a metal-insulator transition by decreasing the bare conductance of the matrix, which controls the transport properties of the composite granular material. On the other hand, the annealing would improve the crystallinity of the Pt grains as well as reduce the carbon content, hence increasing their conductance [34]. The results obtained were interpreted in terms of Coulomb blockade effect re-normalized in presence of a conductive matrix. Furthermore, they showed that for a high enough conductivity, a (granular) metallic conduction was measured, while an insulating behavior was observed in samples with lower conductivity.

In conclusion, a comparison of these results with the ones presented in section 2.1 indicates that the conduction mechanism in Pt-nanowires deposited via FB techniques is governed by the carbonaceous matrix with embedded disordered metallic grains. The details in the temperature behavior depend mainly on the achieved effective doping and disorder level. Other purification processes like annealing in gas atmosphere, post-growth electron irradiation, and deposition on hot substrates were also used; for a review on this topic see [46].

2.2.2 Magnetic deposits

The possibility to produce nanostructures using FB techniques and applied them as sensors increased the interest of growing magnetic nanostructures. Therefore, the EBID of Co and Fe has been intensively studied. Starting with the case of Co, high-quality nanowires have been produced using EBID [47]. These deposits are preferred to the IBID ones (although the later show a resistivity closer to the bulk values) because the Ga+-ion implantation and the produced disorder are not desirable [12,18]. Fernandez-Pacheco et al. [47] found the adequate parameters to produce nanowires with ~80% at. Co, with a resistivity of ~40 μΩ cm at room temperature, using $Co_2(CO)_8$ as the precursor material. This high metal content resulted in a metallic dependence of the resistance at 25 K ≤ T ≤ 300 K. The Hall effect resistivity has been also investigated and it showed two contributions: the anomalous Hall effect at low fields (ρ_{AH}), which increased until a saturation was reached, and the ordinary linear part at higher fields (ρ_{OH}). This behavior has also been observed in polycrystalline Co films [48]. From the slope of the ordinary part the density of electrons at 2 K was estimated n = 7×10^{-28} m^{-3}. This value together with the value of the resistivity at low temperature allowed an estimate of the mean free path $\approx$ 4 nm [48]. As this value is of the order of the grain size it seems reasonable to assume that the scattering is produced mainly at the grain boundaries between crystalline grains. The analysis of the anomalous part showed a dependence $\rho AH \propto \rho^2$ and a value of the saturation magnetization M_s = 1329 ± 20 emu cm^{-3}, which corresponds to 97% of the bulk Co value.

Magnetoresistance studies were performed in three different geometries: magnetic field (H) perpendicular to the substrate plane (perpendicular geometry), H in plane and parallel to the current I (longitudinal geometry), H in plane and perpendicular to I (transversal geometry). The authors reproduced the results of previous publications on Co nanowires [49]. The results of the MR together with the metallic conduction and saturation magnetization were close to the bulk Co values, opening the way for future applications using these nanomagnetic deposits. Additionally, if the growth parameters were modified (except the precursor gas), the content of Co was reduced to ~80% and, hence, all the electrical and magnetic properties changed radically [47]. The room temperature resistivity value was more than 300 times larger than in the case of the nanowires grown under high currents and the ρ(T) curves indicated a slightly semiconducting behavior and the MR decreased by one order of magnitude.

Iron is the second most studied material studied in the form of nanostructures deposited by EBID. Lavrijsen et al. [50] investigated the effect of the content of oxygen and iron in EBID produced wires (using $Fe_2(CO)_9$ as gas precursor) and the consequences on the resistivity. As shown in previous works [47,53], the use of higher currents resulted in higher Fe content. Moreover they successfully varied the Fe/O content (Fe between ~50% and 80%) keeping the carbon content constant (~16%) by adding

H_2O during the deposition. As expected, an increase in resistivity was found as the Fe content decreased and the O content increased. Large amount of Fe (> 70%) led to resistivity values below 100 μΩ cm, as expected for metallic systems. The limit of metallic percolation has been found at Fe content of 70%. If the Fe content was reduced (< 55%), the resistivity was larger than 1000 μΩ cm, close to known values of magnetite, i.e. a poorly conducting material. Intermediate contents of Fe showed a mixture of regions dominated by one or the other of the just mentioned structures. They studied the MR and a typical ferromagnetic behavior was observed, but with a strong dependence on the sample resistivity [50]. For the low resistive samples a clear anisotropic magnetoresistance (AMR) was observed, while in the case of high resistivity sample an intergranular MR was observed, a MR typically found in granular FeO_x systems and explained in terms of tunneling current and/or hopping between magnetic grains [54].

This strong dependence of the metallicity of the Fe deposits on the Fe content was further investigated in [51], where $Fe_2(CO)_9$ was also the gas precursor used. The existence of a disordered metal to insulator transition was observed in the ρ(T) curves depending on the amount of Fe in the structures, Fig. 4a. The ρ(T) curves of the microwires with the highest resistivity follow a $\rho(T) \sim \rho_0 \exp(\frac{T_0}{T})^{1/2}$, indicating clearly that the dominating conducting mechanism is VRH of electrons between localized states. On the contrary, samples with ρ(300 K) ~ 186-526 μΩ cm, showed a ρ(T) behavior characteristic of bad metals. Finally, samples with ρ(300 K) ~ 658-2082 μΩ cm showed a temperature dependence, which combines both metallic and hopping conduction. The conductivity was

progressively degraded as the Fe content decreased, approaching an insulating phase for lower Fe content. As expected, the magnetic properties also changed drastically as a function of the Fe content. The MR was found to have two contributions: the AMR effect and the ITMR (intergranular tunnel magnetoresistance). The higher the content of Fe, the more important was the AMR contribution. Consequently, the lower the Fe content the more important the ITMR contribution. One of the interesting results of the Fe-wires obtained by Córdoba et al. [51] was that they showed a giant anomalous Hall effect far larger than for pure-Fe nanowires. The heterogeneous structure of the wires has been related to this result as well as, according to the authors of that study, a subtle interplay between contributions from spin-dependent and spin-independent scattering [51].

A nearly pure metallic Fe nanowire was successfully produced by Porrati et al. [52] by a combined technique using the EBID and autocatalytic growth from the iron pentacarbonyl ($Fe(CO)_5$) precursor gas under ultra-high vacuum conditions. A high metallicity, Fig. 4b, was reflected also in the results of the Hall resistivity and the MR, as they are in agreement with the investigations on Fe thin films reported in the literature.

2.2.3 Other elements

Other nanostructures containing metals such as palladium or tungsten have been published in the literature. For example, Spoddig et al. [38] studied Pd-EBID deposited wires with low Pd content (~2-6 at.%) compared with the same Pd wires grown with IBID (~16-27 at.%). The
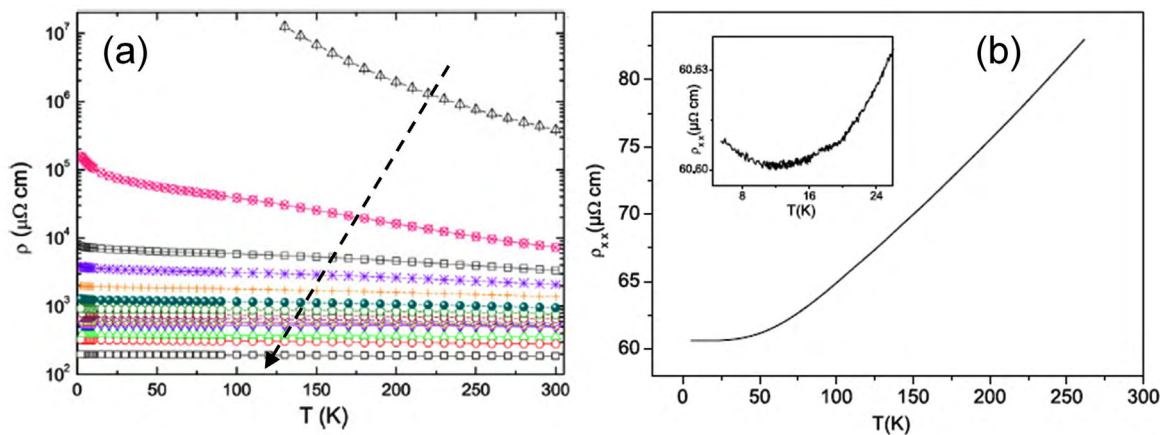
Figure 4: a) Disordered metal to insulating transition showed in the resistivity vs. temperature curves for Fe:O-nanowires deposited using EBID and $Fe_2(CO)_9$ as gas precursor, as described in [50]. The arrow goes from the wires with lowest Fe content (highly resistive) to the Fe-rich ones (lower resistivity). Adapted from [51]; b) resistivity vs. temperature of a Fe microwire. The inset shows the data below 12 K where the resistivity slightly increases. Taken from [52].

high carbon amount present in the Pd-EBID wires (81-90 at.%) appeared to dominate the transport properties and the resistivity temperature dependence revealed a clear semiconducting behavior [38]. Moreover, the resistance increased to the range of several MΩ, suggesting that IBID deposited PdC nanowires were insulating. A similar behavior was found for tungsten-carbide (WC) nanostructures deposited using EBID. Therefore, in the next section we discuss only the properties obtained for WC nanowires prepared by IBID.

3 Superconducting tungsten-carbide nanostructures

3.1 General Characteristics and IBID capabilities

One superconducting nanostructure that can be synthesized by IBID is tungsten-carbide (WC), which shows a critical temperature around 5 K [38,55-57] with an upper critical field $B_{c2}(T = 0.75T_c) \sim 6T$ [38]. Tungsten carbide can have different crystalline phases, e.g. a high temperature fcc phase, low temperature hexagonal WC phase, and a hexagonal W_2C phase, this last superconducting with $T_c = 2.7$ K [58]. According to the literature, the superconducting critical temperature of the WC system depends on the degree of structural disorder, reaching the highest Tc in the amorphous or highly disordered state. Recently done FIB chemical vapor deposition studies of WC nanowires using different precursor mixtures of $C_{14}H_{10}$ and $W(CO)_6$ at different gas temperatures reached the highest Tc ~5.8 K [59].

Information on the elemental composition of usual WC nanostructures deposited by IBID can be seen in [16,38,60]. A typical temperature dependence of a WC superconducting nanostructure is shown in Fig. 5. As expected from the critical temperature value, the atomic structure of the WC deposition shown in Fig. 5, is similar to an amorphous one according to electron diffraction studies [16].

The characterization of the superconducting energy gap and vortex lattice characteristics of a WC 200 nm thick film with an area of ~10^3 µm² was reported in [61], a study that showed that the superconducting properties at the surface of these deposits are very homogeneous, down to an atomic scale. According to that study, the superconducting gap follows the conventional s-wave BCS theory, and scanning tunneling microscopy images under magnetic fields showed a hexagonal vortex lattice [61]. In this section, we will not further review the homogeneous

properties of WC superconducting nanostructures but some of the non-homogeneous ones.

As example of the deposition capabilities of IBID, we show in Fig. 6 two scanning electron microscope images of a WC ring of about 2 µm average diameter and 150 nm thickness and 450 nm width [62]. The ring shown here, for purposes that will become clear below, was produced in a two-step IBID procedure. It consists in re-deposition of WC material on the top of the already deposited superconducting ring path, which are used as the electrical contacts of the ring [62]. We note that with the appropriate current and temperature of the deposition the material created just between the superconducting electrodes and the ring can show a lower critical temperature as the one of the ring itself. This is because the critical temperature is at maximum for the pure amorphous state of the WC alloy and it decreases with annealing and partial crystallization. Another example of the IBID capability for producing WC superconducting structures can be seen in Fig. 7 [60]. In order to study the point contact resistance and the Andreev scattering of a superconductor with a
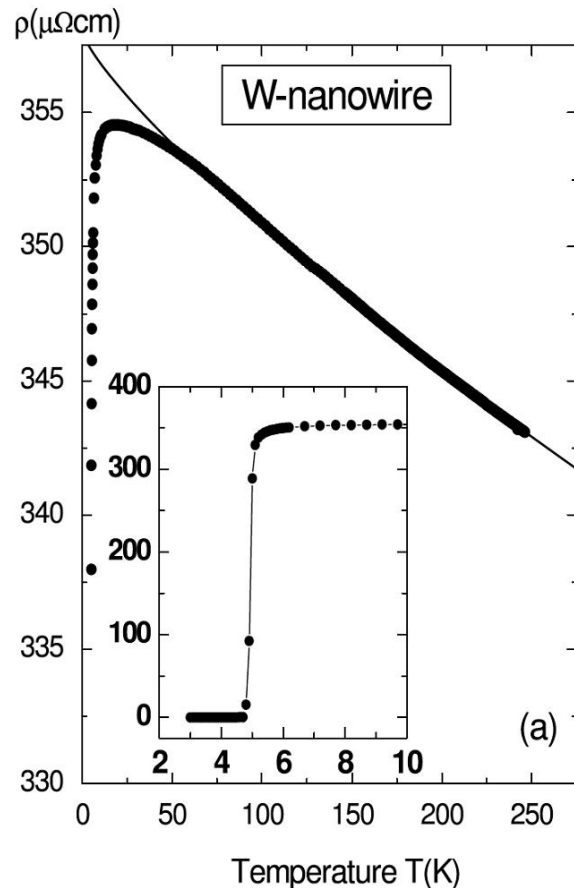
Figure 5: Resistivity vs. temperature at zero applied field for a WC nanowire of dimension (length × width × thickness) 4.5 × 0.17 × 0.13 µm³. The continuous line follows the function $\rho(T) = 358 - 0.182T^{0.8}$ µΩ cm. Inset shows the superconducting transition. Taken from [16].
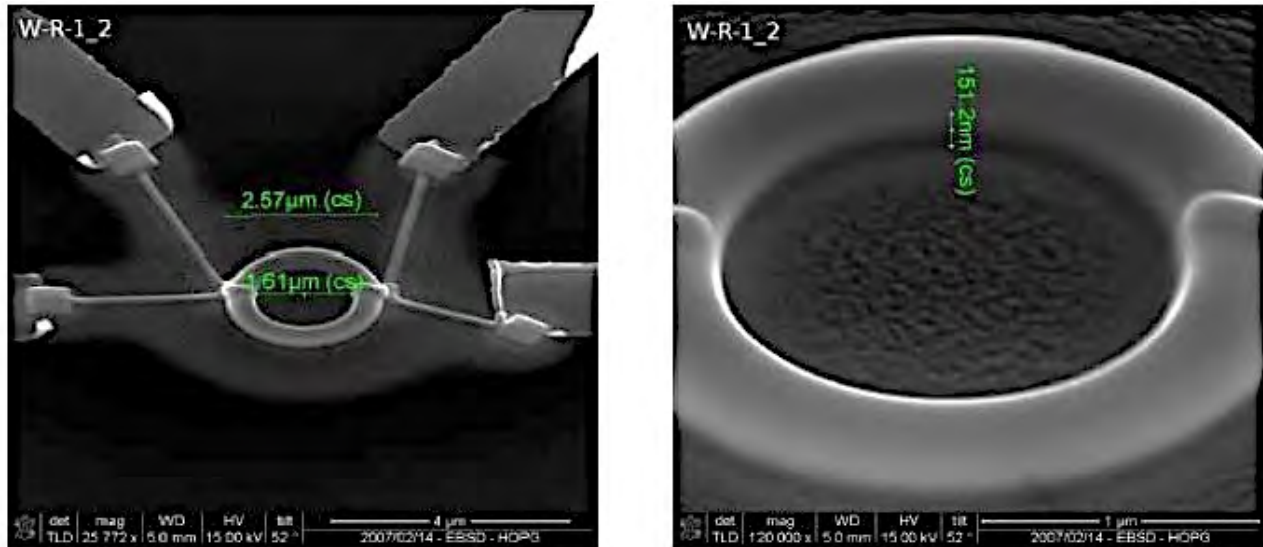
Figure 6: SEM images of a WC ring produced by IBID with its four electrical contacts produced with the same material. Adapted from [62]
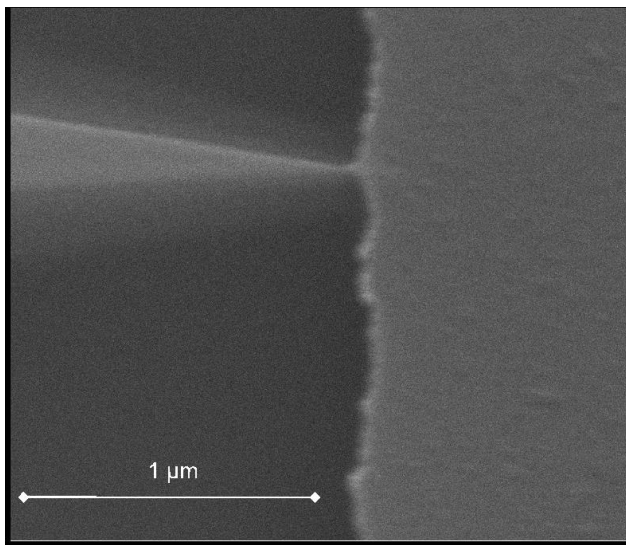
Figure 7: Scanning electron microscopy image under 52° of the WC$_x$ point contact (left) produced by IBID on a Co film surface (right). Adapted from [60].

ferromagnetic material, the end of the WC nanowire in contact to the Co metal film under investigation was made in a needle shape such that the nearly circular contact area had a diameter between 10–20 nm [60].

3.2 Quantum mechanical interference and granular superconductivity effects

We are especially interested on two phenomena, namely periodic field oscillations in the MR – in clear contrast to the 1/B dependence of the Shubnikov-de Haas effect – and an anomalous magnetic field hysteresis loops. We note that these phenomena were also found recently in graphite flakes [63,64] and are generic of granular superconductors.

They can be observed in any superconducting sample within the superconducting transition, where a mixture of normal and superconducting regions is expected. We review here these two phenomena observed in especially prepared WC nanostructures.

3.2.1 Oscillations in the Magnetoresistance of Superconducting-Normal Nanostructures

The main concepts to understand the quantum oscillations in the magnetoresistance follow the model and equations described in [62] and references cited therein. A mixture of superconducting and normal parts with sharp interfaces between them, as depicted in the sketch of Fig. 8, can act as a Fabry-Perot interferometer for electrons if the electronic wave function within the intermediate region M2 behaves coherently having multiple reflections. In this simple one dimensional potential model, the barrier U_2 at M2 has a length L_2. Quantum mechanical resonances in the voltage appear in every nanostructure composed by different materials, if the electronic conduction is ballistic and the roughness of the interfaces is small enough. Therefore, one may observe this effect in case M2 is a normal material if its length is short enough to assure either ballistic transport within it or it is comparable with the carriers' Fermi wave length. The other case is taking M2 as a superconductor.

The parameter U that changes the transmittivity, in case M2 is normal conducting and M1 superconducting, or the Andreev conductance gNS, in case M2 is

superconducting and M1 normal conducting, is included in the potential drop $U_2(x) \sim U_0 - (\frac{U}{L_2})(x - L_1)$ across M2. The potential U is the parameter one changes, either through the input current across the three layer system, or also by applying a magnetic field at constant current in a system with a finite magnetoresistance. The numerical results from [62], Fig. 8, indicate that oscillations will be observed in the transmittivity and/or conductance changing the field or input current. The theoretical solution for the current, in case M2 is superconductor with an energy gap Δ, can be seen in Fig. 9. One obtains clear oscillations in I, which are of larger amplitude at U < Δ than at higher U because in the last case the current is controlled mainly by quasiparticles. A behavior similar to an all-normal conducting M1-M2-M1 system is then expected for U ≥ 3Δ [65-67].

An experimental verification of the above theoretical curve can be obtained by producing a short normal conducting slit in a superconducting WC strip, i.e. a SNS-type nanostructure, for example see sketch in Fig. 9 and the SEM picture above. To reduce the critical current of the WC part and proximity effects at the slit, a magnetic field of 0.25 T was applied [62]. Note that the obtained theoretical results indicate that the measured voltage near the slit will oscillate as a function of current (or as a function of magnetic field at constant current since V(B) = IR(B) ∝ U(B)/e, where R(B) is usually the non-oscillatory magnetoresistance of the sample). The voltage

measurements at the slit from [62], Fig. 9, showed an oscillatory behaviour near the transition to the normal state, with an amplitude of the order of mV. This amplitude agrees with the one expected for a normal conducting region of length of the order of 30 nm. According to the model the increment of the applied voltage drop ΔV needed to obtain one oscillation is [62]:

$$\Delta V \sim \pi^2(\hbar^2/m)(1/L_2^2) \qquad (1)$$

Oscillations of the voltage of similar amplitude but as a function of magnetic field have been also observed in the same channel [62]. Note that the oscillation amplitude
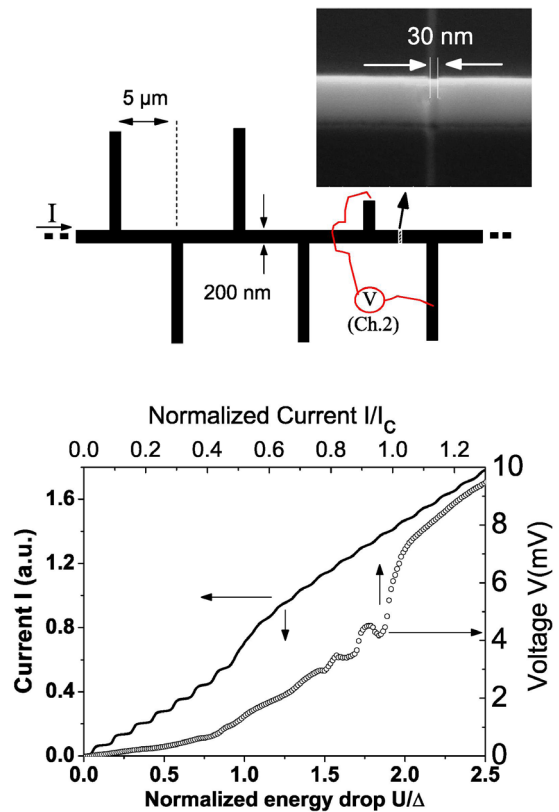
Figure 9: The upper picture shows a sketch of a WC superconducting long strip with a distance of 5 μm between voltage electrodes and a 30 nm long normal conducting slit prepared along the strip using the Ga+ ion irradiation to crystallize the amorphous WC material, see SEM picture on top. Bottom figure: (left-bottom axes) numerical simulation of the carrier current I vs. normalized energy drop at M2, if M2 is a superconductor with energy gap Δ. The carrier current was calculated using the results shown in Fig. 8. Right-top axes: voltage vs. normalized input current obtained in a superconducting strip with a normal conducting slit shown above (Ch.2 in the sketch) at 3.6 K. A magnetic field of 0.25 T was applied normal to the input current and the critical current Ic is the one corresponding to the temperature and applied field of the measurements. Adapted from [62]

Figure 8: For a one-dimensional three-layer strip system M1-M2-M1 (see the inserted sketch) the main panel shows the transmittivity T vs. normalized energy drop within an interlayer M2 in the normal state (dashed red line). The continuous line shows the Andreev conductance g_{NS} vs. normalized energy drop for a superconducting interlayer M2. Insert: E is the incoming particle energy, U_0 is the potential height at M2 at the left interface with M1 and $U_2(x)$ is the position-dependent potential function that depends on the applied potential drop U. Adapted from [62].

of the order of mV is larger than the superconducting gap of the strip. At the temperature of the measurements $\Delta(3.6\ K) \approx 0.45$ meV [61], i.e. the situation in the measured structure is similar to a trilayer with normal conducting materials.

A further verification of the model predictions, especially Eq. 1, can be done experimentally by choosing a trilayer system with a longer M2 superconducting region, i.e. changing substantially the length L_2 in comparison with the 30 nm length used before. This has been realized with the above described superconducting ring of Fig. 6.

The ring itself represents two M2 superconducting regions in parallel. To get the normal conducting regions M1 contacting the ring, one deposits a second time the WC material on the top of the ring. In this case and due to a partial irradiation and annealing of the already deposited superconducting material, the critical temperature decreases in comparison with that of the ring. Therefore we expect a NSN system in a restricted range of temperature and magnetic field, as the temperature and field dependence of the ring structure reveals, Fig. 10a. The oscillations in the magnetoresistance shown in Fig. 10b are observed in a restricted region of field and temperature. Superconducting rings without the double IBID procedure did not show these oscillations [62]. The oscillations amplitude is of the order of 50 neV (note that the resistance is of the order of 1 Ω and the input current is 1 μA), in very good agreement with the value predicted by Eq. 1 if $L_2 \approx 3\ \mu$m. We would like to emphasize an important remark done in [62]: this oscillation amplitude is much smaller than the thermal energy of 0.4 meV, implying that the normal conducting M1 regions should be a narrow gap semiconductor, otherwise the thermally excited electrons would not allow to observe the small oscillations in the 50 neV range. Indeed, the temperature dependence of the resistance in the normal state of the WC structures is not metallic, Fig. 5.

All the details we learned from those experiments indicated that for the observation of the quantum oscillations several conditions are needed regarding the length of the M2 part, the electronic properties of both parts and the interfaces between them. Therefore, one should not be surprised if the oscillations are observed only at certain temperature and field range of a superconducting transition. In general the temperature region very near or within a superconducting transition is predestined to the observation of these quantum oscillations. Similar quantum oscillations to those described in this subsection were observed in granular Pb and Al thin films near the percolation threshold and at temperatures and fields in the vicinity of the transition [68]. The observed effects in

the thin film can be well described by the one-dimensional model presented in [62]. The amplitude of the voltage oscillations with field at constant current as well as the increasing amplitude of these oscillations increasing the input current can be quantitatively understood taking into account the typical size of the normal-superconducting regions shown in [68] using the concepts discussed in this section.

3.2.2 Anomalous Field Hysteresis Loops in Superconducting-Normal Nanostructures

Granular superconductivity can be found in samples in which the superconducting grains are embedded in a non-superconducting matrix. At low enough temperatures
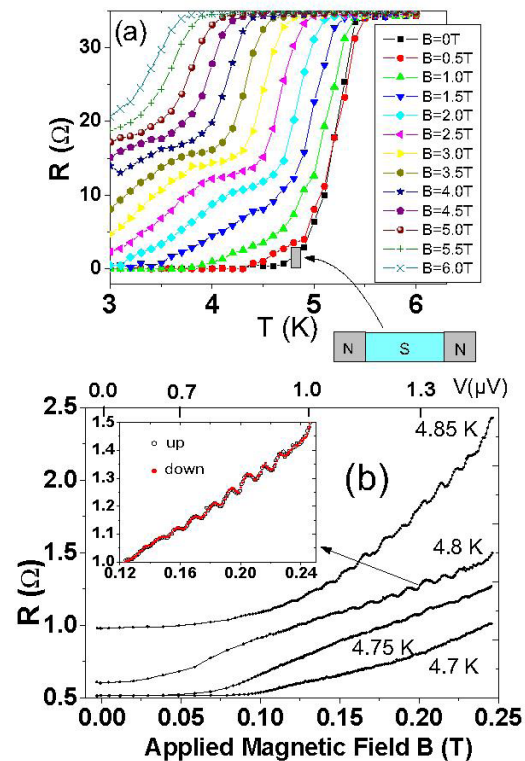
Figure 10: a) Resistance of the ring shown in Fig. 6 as a function of temperature at constant magnetic fields applied normal to the main area. The small rectangle and the sketch at the bottom of the figure indicate the region where the sample consists of normal electrodes and the superconducting path along the ring. According to the used model this system is necessary to understand the quantum oscillations observed in the magnetoresistance shown in b) at different constant temperatures. The inset in b) shows the magneto-resistance sweeping up and down the magnetic field. The absence of irreversibility indicates that heating effects are not relevant. The measurements were done at a constant current of 1 μA $\ll I_c$, the critical current at the relevant temperatures and magnetic fields. Taken from [62]

and input currents, the main transport mechanism that influences the measured electrical resistance of a granular superconducting system is the tunnelling of Copper pairs between the superconducting grains via the Josephson effect, if the potential barrier between them does allow. Depending on the system under study, the resistance may vanish at low enough temperatures and input currents below the Josephson critical current. We note that the first high-temperature superconducting (HTSC) oxide samples showed typical signs for granular superconductivity and their resistance did not vanish [69].

The behavior of the magnetization of transport properties of a system that shows granular superconductivity is in general complex and is well described in the literature of the 80's [70,71] and 90's [72,73]. In this section and using similar samples presented in the last section, we shall discuss another particular effect that appears as a fingerprint of granular superconductivity, namely an anomalous hysteresis loop in the magnetoresistance.

The magnetoresistance of a granular superconducting sample with finite pinning of vortices (or fluxons generated within the Josephson medium) and finite Josephson coupling between the grains, shows an anomalous field hysteresis, being the resistance smaller, coming from higher fields, than the resistance measured increasing field, and vice versa in the other

field direction, see, e.g., [64,73–76]. The explanation in terms of the two-level (or two-Bean) model has been given in [73] assuming a finite critical current within the Josephson medium and a different one within the superconducting grains.

Fig. 11a shows a SEM picture of a WC nanowire in which a change of the wire width has been produced during a two-step deposition. Similar to the examples discussed above, such deposition causes at the constriction a superconducting region with a slightly lower critical temperature than the rest of the wire. This can be observed by measuring the resistance as a function of temperature at different applied fields, Fig. 11b. Using the other voltage electrodes one can check that this behavior is only observed in the constriction region indicated by the arrow in Fig. 11a. In this case and fixing the temperature in the region where the lower critical temperature part remains in the normal state (localized by the arrow in Fig. 11b), one expects to have a granular superconducting system. Indeed, the magnetoresistance hysteresis loop at 3.85 K, Fig. 11c, shows the expected anomalous hysteresis loop in the magnetoresistance. Note also the clear difference in the MR slope for fields below and above 5 mT, Fig. 11c. As expected these main granular superconducting characteristics vanish at temperatures below 3.8 K, where all the sample is superconducting.
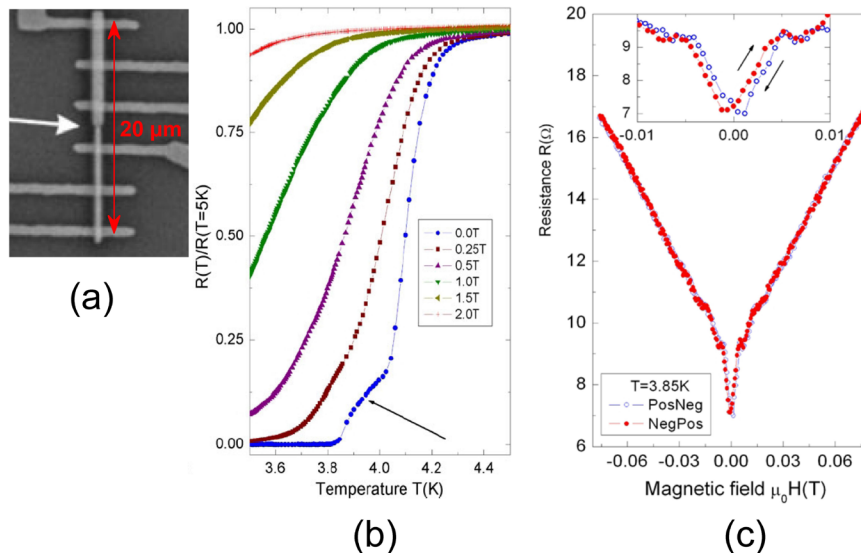
Figure 11: a) WC nanowire produced with IBID in two steps with a change in the wire width, as indicated by the arrow; b) temperature dependence of the normalized resistance at different applied fields from the region with the constriction, 11a. Granular superconducting behavior was observed in the temperature region shown by the arrow; c) Field dependence of the resistance at T = 3.85 K obtained in two field sweep directions, as indicated by the different color symbols. The inset blows out the low field region where a clear anomalous field hysteresis was measured. Adapted from [60].

References

[1] Van Dorp W. F., Hagen C. W., A critical literature review of focused electron beam induced deposition, J. App. Phys., 2008, 104, 08130.

[2] Utke I., Hoffmann P., Melngailis J., Gas-assisted focused electron beam and ion beam processing and fabrication, Journal of Vacuum Science & Technology B, 2008, 26, 1197-1276.

[3] Gabureac M., Bernau L., Utke I., Boero G., Granular CoC nano-Hall sensors by focused-beam-induced deposition, Nanotechnology, 2010, 21, 115503.

[4] Dhakal P., McMahon G., Shepard S., Kirkpatrick T., Oh J. I., Naughton M. J., Direct-write, focused ion beam-deposited, 7 K superconducting C-Ga-O nanowires, Appl. Phys. Lett., 2010, 96, 262511.

[5] Weirich P. M., Schwalb C. H., Winhold M., Huth M., Superconductivity in the system MoxCyGazOδ prepared by focused ion beam induced deposition, Journal of Applied Physics, 2014, 115, 174315.

[6] De Teresa J. M., Córdoba R., Fernández-Pacheco A., Montero O., Strichovanec P., Ibarra M. R., Origin of the Difference in the Resistivity of As-Grown Focused-Ion- and Focused-Electron-Beam-Induced Pt Nanodeposits, Journal of Nanomaterials 2009, 936863.

[7] Mott N. F., Davis E. A., Electronic Processes in Non-Crystalline Materials, Clarendon Press, Oxford, UK, 1979.

[8] Möbius A., Frenzel C., Thielsch R., Rosenbaum R., Adkins C. J., Schreiber M., Bauer H.-D., Grötzschel R., Hoffmann V., Krieg T., et al., Metal-insulator transition in amorphous Si1-xNix: evidence for Mott's minimum metallic conductivity, Phys. Rev. B, 1999, 60, 14209-14223.

[9] Arena C., Kleinsorge B., Robertson J., Milne W. I., Welland M. E., Hopping conductivity in disordered systems, App. Phys., 1999, 85, 1609-1615.

[10] Prasad V., Magnetotransport in the amorphous carbon films near the metal-insulator transition, Solid State Communications, 2008, 145, 186-191.

[11] Lin J. F., Bird J. P., Rotkina L., Sergeev A., Mitin U., Large effects due to electron-phonon-impurity interference in the resistivity of Pt/C-Ga composite nanowires, App. Phys. Lett., 2004, 84, 3828-3830.

[12] Lin J. F., Bird J. P., Rotkina L., Bennett P. A., Classical and quantum transport in focused-ion-beam-deposited Pt nanointerconnects, App. Phys. Lett., 2003, 82, 802-804.

[13] Lin J. F., Bird J. P., Rotkina L., Low-temperature decoherence in disordered Pt nanowires, Physica E, 2003, 19, 112-116.

[14] Lin J. F., Bird J. P., Recent experimental studies of electron dephasing in metal and semiconductor mesoscopic structures, J. Phys. Condens. Matter, 2002, 14, 501-596.

[15] Echternach P. M., Gershenson M. E., Bozler H. M., Bogdanov A. L., Nilsson B., Temperature dependence of the resistance of one-dimensional metal films with dominant Nyquist phase breaking, Phys. Rev. B, 1994, 50, 5748-5751.

[16] Barzola-Quiquia J., Schulze S., Esquinazi P., Transport properties and atomic structure of ion-beam-deposited W, Pd and Pt nanostructures, Nanotechnology, 2009, 20, 165704.

[17] Wakaya F., Tsukatani Y., Yamasaki N., Murakami K., Abo S., Takai M., Transport Properties of Beam-Deposited Pt Nanowires, J. Phys.: Conference Series, 2006, 38, 120-215.

[18] Peñate-Quesada L., Mitra J., Dawson P., Non-linear electronic transport in Pt nanowires deposited by focused ion beam, Nanotechnology, 2007,18, 215203.

[19] Liao Z. M., Xu J., Zhang X. Z., Yu D. P., The relationship between quantum transport and microstructure evolution in carbon-sheathed Pt granular metal nanowires, Nanotechnology, 2008, 19, 305402.

[20] Fernández-Pacheco A., De Teresa J. M., Córdoba R., Ibarra M. R., Metal-insulator transition in Pt-C nanowires grown by focused-ion-beam-induced deposition, Phys. Rev. B, 2009, 79, 174204.

[21] Glazman L. I. , Matveev K. A., Inelastic resonant tunneling of electrons through a potential barrier, Sov. Phys. JETP, 1988, 67, 163.

[22] Marzi G. D., Iacopino D., Quinn A. J., Redmonda G., Probing intrinsic transport properties of single metal nanowires: Direct-write contact formation using a focused ion beam, J. App. Phys., 2004, 96, 3458-3462.

[23] Dynes R. C., Garno J. P., Metal-Insulator Transition in Granular Aluminum, Phys. Rev. Lett., 1981, 46, 137-140.

[24] Ravindranath V., Rao M. S. R., Rangarajan G., Lu Y., Klein J., Klingeler R., Uhlenbruck S., Büchner B., Gross R., Magneto-transport studies and mechanism of Ho- and Y-doped La0.7Ca0.3MnO3, Phys. Rev. B, 2011, 63, 184434-184441.

[25] Shafarman W. N., Koon D. W., Castner T. G., DC conductivity of arsenic-doped silicon near the metal-insulator transition, Phys. Rev. B, 1989, 40, 1216-1231.

[26] Delahaye J., Brison J. P., Berger C., Evidence for Variable Range Hopping Conductivity in the Ordered Quasicrystal i-AlPdRe, Phys. Rev. Lett., 1998, 81, 4204-4207.

[27] Anderson P. W., Absence of Diffusion in Certain Random Lattices, Phys. Rev., 1958, 109, 1492-1505.

[28] Langford R. M., Wang T.-X., Ozkaya D., Reducing the resistivity of electron and ion beam assisted deposited Pt, Microelectronic Engineering, 2007, 84, 784-788.

[29] McLachlan I., Rosenbaum R., Albers A., Eytan G., Grammatica N., Pickup J., Zaken E.,The temperature and volume fraction dependence of the resistivity of granular Al-Ge near the percolation threshold, J. Phys. Condens. Matter., 1993, 5, 4829.

[30] Sharma S. N., Shivaprasad S. M., Kohli S., Rastogi A., Substrate temperature dependence of electrical conduction in nanocrystalline CdTe:TiO2 sputtered films, Pure Appl. Chem., 2002, 74, 1739-1749.

[31] Stiller M., Barzola-Quiquia J., Lorite I., Esquinazi P., Kirchgeorg R., Albu S., Schmuki P., Transport properties of single TiO2 nanotubes, Appl. Phys. Lett., 2013, 103, 173108.

[32] Lee P. A., Ramakrishnan T. V., Disordered electronic systems, Rev. Mod. Phys., 1985, 57, 287-337.

[33] Liao Z. M., Xu J., Song Y. P., Zhang Y., Xing Y. J., Yu D. P., Quantum interference effect in single Pt(Ga)/C nanowire, Appl. Phys. Lett., 2005, 87, 182112.

[34] Rotkina L., Oh S., Eckstein J. N., Rotkin S. V., Logarithmic behavior of the conductivity of electron-beam deposited granular Pt/C nanowires, Phys. Rev. B, 2005, 72, 233407.

[35] Altland A., Glazman L. I., Kamenev A., Electron Transport in Granular Metals, Phys. Rev. Lett., 2004, 92, 026801.

[36] Feigel'man M. V., Ioselevich A. S., Skvortsov M. A., Quantum Percolation in Granular Metals, Phys. Rev. Lett., 2004, 93, 136403.

[37] Blanter Y. M., Vinokur V. M., Glazman L. I., Weak localization in metallic granular media, Phys. Rev. B, 2006, 73, 165322.

[38] Spoddig D., Schindler K., Rödiger P., Barzola-Quiquia J., Fritsch K., Mulders H., Esquinazi P., Transport properties and growth parameters of PdC and WC nanowires prepared in a dual-beam microscope, Nanotechnology, 2007 18, 495202.

[39] Efros A. L., Shklovskii B. I., Coulomb gap and low temperature conductivity of disordered systems, J. Phys. C: Solid State Phys., 1975, 8, L49.

[40] Shedd G. M., Lezec H., Dubner A. D., Melngailis J., Focused ion beam induced deposition of gold, App. Phys. Lett., 1986, 49, 1584-1586.

[41] Fransson J., Lin J.-F., Rotkina L., Bird J. P., Bennett P. A., Signatures of bandlike tunneling in granular nanowires, Phys. Rev. B, 2005, 72, 113411.

[42] Aladashvili D. I., Adamiya Z. A., Lavdovskii K. G., Levin E. I., Shklovskii B. I., Negative differential resistance in the hopping conductivity region in silicon, JETP Letters, 1988, 47, 466-469.

[43] Mel'nikov A. P., Gurvich Y. A., Shestakov L. N., Gershenzon E. M., Magnetic field effects on the nonohmic impurity conduction of uncompensated crystalline silicon, JETP Letters, 2001, 73, 44-47.

[44] Tsukatani Y., Yamasaki N., Murakami K., Wakaya F., Takai M., Transport Properties of Pt Nanowires Fabricated by Beam-Induced Deposition, Jpn. J. Appl. Phys., 2005, 44, 5683-5686.

[45] Rotkina L., Lin J. F., Bird J. P., Nonlinear current-voltage characteristics of Pt nanowires and nanowire transistors fabricated by electron-beam deposition, App. Phys. Lett., 2003, 83, 4426.

[46] Botman A., Mulders J. J. L., Hagen C. W., Creating pure nanostructures from electron-beam-induced deposition using purification techniques: a technology perspective, Nanotechnology, 2009, 20, 372001.

[47] Fernández-Pacheco A., De Teresa J. M., Córdoba R., Ibarra M. R., Magnetotransport properties of high-quality cobalt nanowires grown by focused-electron-beam-induced deposition, J. Phys. D: Appl. Phys., 2009, 42, 055005.

[48] Kötzler J., Gil W., Anomalous Hall resistivity of cobalt films: Evidence for the intrinsic spin-orbit effect, Phys. Rev. B, 2005, 72, 060412.

[49] Leven B. , Dumpich G., Resistance behavior and magnetization reversal analysis of individual Co nanowires, Phys. Rev. B, 2005, 71, 064411.

[50] Lavrijsen R., Córdoba R., Schoenaker F. J., Ellis T. H., Barcones B., Kohlhepp J. T., Swagten H. J. M., Koopmans B., De Teresa J. M., Magén C., et al, Fe:O:C grown by focused-electron-beam induced deposition: magnetic and electric properties, Nanotechnology, 2011, 22, 025302.

[51] Córdoba R., Lavrijsen R., Fernández-Pacheco A., Ibarra M. R., Schoenaker F., Ellis T., Barcones-Campo B., Kohlhepp J. T., Swagten H. J. M., Koopmans B., et al., , Giant anomalous Hall effect in Fe-based microwires grown by focused-electron-beam-induced deposition, J. Phys. D: Appl. Phys., 2012, 45, 035001.

[52] Porrati F., Sachser R., Walz M. M., Vollnhals F., Steinrück H. P., Marbach H., Huth M., Magnetotransport properties of iron microwires fabricated by focused electron beam induced autocatalytic growth, J. Phys. D: Appl. Phys., 2011, 44, 425001.

[53] Córdoba R., Sesé J., De Teresa J. M., Ibarra M. R., High-purity cobalt nanostructures grown by focused-electron-beam-induced deposition at low current, Microelectron. Eng., 2010, 87, 1550-1553.

[54] Ziese M., Extrinsic magnetotransport phenomena in ferromagnetic oxides, Rep. Prog. Phys., 2002, 65, 143-249.

[55] Sadki E. S., Ooi S., Hirata K., Focused-ion-beam-induced deposition of superconducting nanowires, Appl. Phys. Lett., 2004, 85, 6206.

[56] Li Y., Sinitskii A., Tour J., Electronic two-terminal bistable graphitic memories, Nature Mater., 2008, 7, 966-971.

[57] Luxmoore I. J., Ross I., Cullis A., Fry P., Orr J., Buckle P., Jefferson J., Low temperature electrical characterization of tungsten nano-wires fabricated by electron and ion beam induced chemical vapor deposition, Thin Solid Films, 2007, 515, 6791-6797.

[58] Willens R. H., Buehler E., The superconductivity of the monocarbides of Tungsten and Molybdenum, Appl. Phys. Lett., 1965, 7, 25.

[59] Dai J., Onomitsu K., Kometani R., Krockenberger Y., Yamaguchi H., Ishihara S., Warisawa S., Superconductivity in Tungsten-Carbide Nanowires Deposited from the Mixtures of W(CO)6 and C14H10, Jpn. J. Appl. Phys., 2013, 52, 075001.

[60] Barzola-Quiquia J., Dusari S., Chiliotte C., Esquinazi P., Andreev reflection and granular superconductivity features observed in mesoscopic samples using amorphous tungsten carbide superconductors, J. Supercond. Nov. Magn., 2011, 24, 463-469.

[61] Guillamón I., Suderow H., Vieira S., Fernández-Pacheco A., Sesé J., Córdoba R., De Teresa J. M., Ibarra M. R., Nanoscale superconducting properties of amorphous W-based deposits grown with a focused-ion-beam, New J. of Phys., 2008, 10, 093005.

[62] Rödiger P., Esquinazi P., García N., Andreev Oscillations in Normal-Superconducting-Normal Nanostructures, J. Supercond. Nov. Magn., 2009, 22, 331-335.

[63] Esquinazi P., García N., Barzola-Quiquia J., Rödiger P., Schindler K., Yao J.-L., Ziese M., ndications for intrinsic superconductivity in highly oriented pyrolytic graphite, Phys. Rev. B, 2008, 78, 134516.

[64] Dusari S., Barzola-Quiquia J., Esquinazi P., Superconducting Behavior of Interfaces in Graphite: Transport Measurements of Micro-constrictions, J. Supercond. Nov. Magn., 2011, 24, 401-405.

[65] Andreev A. F., The Thermal Conductivity of the Intermediate State in Superconductors, Sov. Phys. JETP, 1964, 19, 1228.

[66] Blonder G. E., Tinkham M., Klapwijk T. M., Transition from metallic to tunneling regimes in superconducting microconstrictions: Excess current, charge imbalance, and supercurrent conversion, Phys. Rev. B, 1982, 25, 4515.

[67] Garcia N., Flores F., Guinea F., Theory of tunneling in metal-superconducto devices: Supercurrents in the superconductor gap at zero temperatures, J. Vac. Sci. Technol. A, 1988, 6, 323-326.

[68] Gerber A., Deutscher G., Ac-to-dc Conversion and Aharonov-Bohm Effect in Percolating Superconducting Films, Phys. Rev. Lett., 1990, 64, 1585.

[69] Berdnorz J. G., Müller K. A., Possible high Tc superconductivity in the Ba-La-Cu-O system
Z. Phys. B, 1986, 64, 189-193.

[70] Shapira Y. , Deutscher G., Semiconductor-superconductor transition in granular Al-Ge, Phys. Rev. B, 1983, 27, 4463-4466.

[71] Clem J. R., Granular and superconducting-glass properties of the high-temperature superconductors, Physica C, 1988, 50, 153-155.

[72] Senoussi S., Aguillon C., Hadjoudj S., The contribution of the intergrain currents to the low field hysteresis cycle of granular superconductors and the connection with the micro- and macrostructures, Physica C , 1991, 175, 215-225.

[73] Ji L., Rzchowski M. S., Anand N., Thinkam M., Magnetic-field-dependent surface resistance and two-level critical-state model for granular superconductors, Phys. Rev. B, 1993, 47, 470-483.

[74] Kopelevich Y., dos Santos C., Moehlecke S., Machado A., Current-Induced Superconductor-Insulator Transition in Granular High-Tc Superconductors, 2001, arXiv:0108311.

[75] Felner I., Galstyan E., Lorenz B., Cao D., Wang Y. S., Xue Y. Y., Chu C. W., Magnetoresistance hysteresis and critical current density in granular RuSr2Gd2-xCexCu2O10-δ, Phys. Rev. B, 2005, 67, 134506.

[76] Balaev D. A., Gokhfeld D. M., Dubrovski A. A., Popkov S. I., Shaikhutdinov K., Petrov M. I., Magnetoresistance hysteresis in granular HTSCs as a manifestation of the magnetic flux trapped by superconducting grains in YBCO + CuO composites, Journal of Experimental and Theoretical Physics, 2007, 105, 1174-1183.